

# Robust Brain MRI Image Classification with SIBOW-SVM

Liyun Zeng<sup>1,2</sup> and Hao Helen Zhang<sup>1,2,\*</sup>

<sup>1</sup>Statistics and Data Science GIDP, University of Arizona, Tucson, AZ, 85721, USA

<sup>2</sup>Department of Mathematics, University of Arizona, Tucson, AZ, 85721, USA

\*Corresponding author: hzhang@math.arizona.edu

## Abstract

The majority of primary Central Nervous System (CNS) tumors in the brain are among the most aggressive diseases affecting humans. Early detection of brain tumor types, whether benign or malignant, glial or non-glial, is critical for cancer prevention and treatment, ultimately improving human life expectancy. Magnetic Resonance Imaging (MRI) stands as the most effective technique to detect brain tumors by generating comprehensive brain images through scans. However, human examination can be error-prone and inefficient due to the complexity, size, and location variability of brain tumors. Recently, automated classification techniques using machine learning (ML) methods, such as Convolutional Neural Network (CNN), have demonstrated significantly higher accuracy than manual screening, while maintaining low computational costs. Nonetheless, deep learning-based image classification methods, including CNN, face challenges in estimating class probabilities without proper model calibration (Guo et al., 2017; Kumar et al., 2018; Minderer et al., 2021). In this paper, we propose a novel brain tumor image classification method, called SIBOW-SVM, which integrates the Bag-of-Features (BoF) model with SIFT feature extraction and weighted Support Vector Machines (wSVMs). This new approach effectively captures hidden image features, enabling the differentiation of various tumor types and accurate label predictions. Additionally, the SIBOW-SVM is able to estimate the probabilities of images belonging to each class, thereby providing high-confidence classification decisions. We have also developed scalable and parallelable algorithms to facilitate the practical implementation of SIBOW-SVM for

massive images. As a benchmark, we apply the SIBOW-SVM to a public data set of brain tumor MRI images containing four classes: glioma, meningioma, pituitary, and normal. Our results show that the new method outperforms state-of-art methods, including CNN.

*Key Words and Phrases:* Medical image classification, convolutional neural network (CNN), scale-invariant feature transform (SIFT), support vector machine (SVM), multiclass classification, probability estimation, nonparametric, robust, model calibration, high-performance computing (HPC).

## 1 Introduction

Brain tumors are caused by the abnormal growth of uncontrolled cells within the human brain, and can be categorized as malignant (cancerous) or benign (noncancerous). The major brain tumor types include gliomas, meningiomas, and pituitary tumors. Gliomas originate from glial cells that support neurons, including astrocytes, oligodendrocytes, and ependymal cells, rather than nerve cells and blood vessels. Gliomas are typically malignant, fast-growing, and invasive, and they have the potential to significantly impact brain functions and pose a life-threatening risk (DeAngelis, 2001). In contrast, meningioma arises from meninges which are membranes surrounding the brain and spinal cord, and pituitary tumors are abnormal growths in the pituitary gland located behind the nasal cavity (Johnson et al., 2017). Meningioma and pituitary tumors are typically benign, growing slowly, and typically not spreading to other parts of the body. However, they can sometimes affect nearby brain tissues, nerves, or blood vessels, potentially resulting in severe disabilities and associated medical damages. When brain tumors grow large enough to add pressure on surrounding nerves, blood vessels and tissue, they can affect brain functions and the overall health of patients. Early detection and accurate classification of these tumors are essential for clinical diagnosis and effectiveness in treatment, ultimately leading to improved patient survival rates (Hishii et al., 2019). However, brain tumor screening poses a formidable challenge for human eyes and is susceptible to subjectivity, even for experienced radiologists (Burger and Scheithauer, 1994; Chamasemani and Singh, 2011; Afshar et al., 2019), owing to the physiological complexity of tumors.

Magnetic Resonance Imaging (MRI) scan is one of the most commonly used medical screening procedures for the diagnosis of primary brain tumors (Amin et al., 2020b). Unlike tumors in other parts of the body, collecting a biopsy sample from brain tumors through surgery is a complex and challenging procedure. Consequently, the availability of a dependable confidence measure for classifying brain tumors using MRI image scans is critically important for early diagnosis. In recent years, advancements in computational technology and machine learning methods have significantly improved MRI-based tumor screening (Wernick et al., 2010; Giger, 2018; Currie et al., 2019). Various machine learning techniques designed for computer vision and image classification provide radiologists with abundant information and objective recommendations for tumor classification. Among these methods, Convolutional Neural Networks (CNNs) have gained widespread popularity for their computational efficiency and high accuracy in classifying brain tumor MRI images, thanks to their ability to extract intricate features from images (Sajjad et al., 2019; Baranwal et al., 2020; Febrianto et al., 2020; Iqbal et al., 2018; Hashemzahi et al., 2020; Ayadi et al., 2021). Based on Litjens et al. (2017), there were about 220 research works related to deep learning for medical images in 2016, with 190 of them adopting CNNs as their methodology. Furthermore, the implementation of parallel CNNs on the NVIDIA CUDA GPU architecture has substantially accelerated the processing of massive image data and model training, making CNNs the gold standard for image classification (Li et al., 2016; Gavali and Banu, 2019; Santos et al., 2019; Sultan et al., 2019).

It is widely known that CNNs have achieved remarkable success in classifying massive image data sets such as ImageNet, which boasts over one million images (Russakovsky et al., 2015). However, when it comes to the application of deep CNNs to medical image classification with limited data, significant challenges arise. Training deep CNNs on small data sets tends to lead to overfitting and convergence issues. Hyperparameter tuning adds further computational demands and expenses (Neary, 2018; Wang et al., 2018; Tuba et al., 2021). Furthermore, in the context of brain tumor screening, accurate probability estimation is critical to quantify prediction uncertainty. Recent studies show that deep CNNs may struggle to provide precise probability estimations (Guo et al., 2017; Kumar et al., 2018; Minderer et al., 2021).

A promising alternative lies in the class of weighted Support Vector Machines (wSVMs), an

SVM-based learning approach tailored for probability estimation in problems involving multiple classes, denoted as  $K$  (Wang, Zhang and Wu, 2019). These estimators are flexible, robust and accurate in estimating posterior class probabilities, with the polynomial-time complexity in  $K$ . Recent work by Zeng and Zhang (2022) has introduced two new learning schemes: the baseline learning and the One-vs-All (OVA) learning, to enhance both computational efficiency and probability estimation accuracy for wSVMs. In particular, the baseline learning scheme has the optimal linear complexity, and the OVA scheme stands out for achieving superior estimation accuracy in the numerical studies, compared with other traditional methods such as multinomial logistic regression (MLG), multiclass linear discriminant analysis (MLDA), classification trees (TREE, Breiman et al., 1984), random forest (RF, Ho, 1995), and XGBoost (XGB, Chen and Guestrin, 2016).

In this article, we propose a novel approach based on weighted Support Vector Machines (wSVMs), called **SIBOW-SVM**, for both image classification and probability estimation. The SIBOW-SVM learning framework first extracts image features using the scale-invariant feature transformation (SIFT) technique (Lowe, 1999, 2004), followed by the application of the Bag-of-Feature (BoF) model (Sivic and Zisserman, 2003; Csurka et al., 2004; Hiba et al., 2016) for codebook generation, feature encoding, and pooling. Finally, wSVMs are employed to classify images and estimate class probabilities. Notably, the computational cost of the SIBOW-SVM is comparable to that of CNNs when not utilizing NVIDIA CUDA GPU acceleration. However, its divide-and-conquer nature allows for significant speed-up through parallel computing using GPUs, multi-core processors, high-performance computing (HPC) clusters, and massively parallel computing (MPP) systems. We will evaluate the performance of the SIBOW-SVM on public image data sets and compare its results with other methods, including CNNs.

The remainder of the paper is organized as follows. Section 2 describes the image classification systems and image pre-processing techniques, and introduces the brain tumor MRI image data set. Section 3 presents the proposed SIBOW-SVM methodology, elucidating its computational algorithm and practical implementation details. Section 4 presents and discusses the numerical results, which are followed by the concluding remarks in Section 5.

## 2 Image Classification Systems

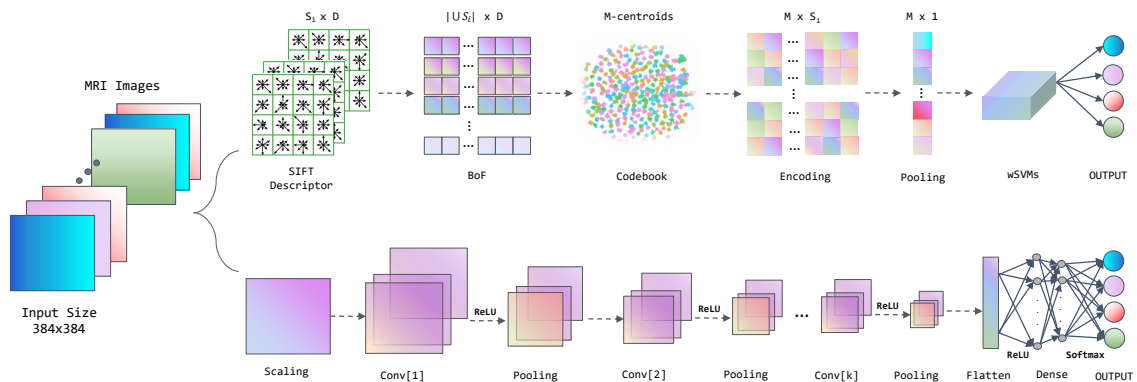
### 2.1 Image Classification Systems

Image classification involves a sequence of systematic steps, from preparing images to building classification models. The first step is image pre-processing, which consists of image labeling and standardization. Standardizing raw images to a uniform pixel size is essential for both model training and cross-method evaluation. Moreover, we randomly split the entire data set into two parts: the training set  $\mathbb{S}_{train}$ , comprising (80%), and the test set  $\mathbb{S}_{test}$ , constituting (20%). These subsets are consistently used to assess and compare different methodologies.

In Figure 1, we illustrate the image classification systems employed in both the CNN network architecture and our proposed SIBOW-SVM. Each system utilizes  $\mathbb{S}_{train}$  for training purposes and  $\mathbb{S}_{test}$  for evaluating performance. The CNN network architecture, detailed in the lower row of Figure 1, begins with scaling pixel values, followed by the application of several convolutional and pooling layers, using ReLU as the activation function. The pooled features are then flattened and fed into a fully connected dense network. This network employs the softmax function to estimate class probabilities. The SIBOW-SVM framework, depicted in the upper row, starts by extracting SIFT features from each image. These features are combined to create a large Bag of Features (BoF) feature pool. The training images are then described through histograms of local descriptors.

The subsequent step is to construct a codebook by clustering the BoF feature pool, for example, using the  $k$ -means algorithm to generate clusters around  $M$  centroids, as a codebook (vocabulary) representing *visual words*. Each image is then encoded using this codebook, resulting in a list of *visual codes* that represent local descriptors. These visual codes can be seen as local histograms of  $M$  dimensions, corresponding to the size of the codebook. The final image feature is an  $M$ -vector, obtained by pooling and normalizing the *visual code* encoding, serving as the input for weighted Support Vector Machines (wSVMs) for classification and probability estimation (Zeng and Zhang, 2022).

Figure 1: Brain tumor MRI image classification systems for the CNN network architecture (in the lower row) and the proposed SIBOW-SVM framework (in the upper row).



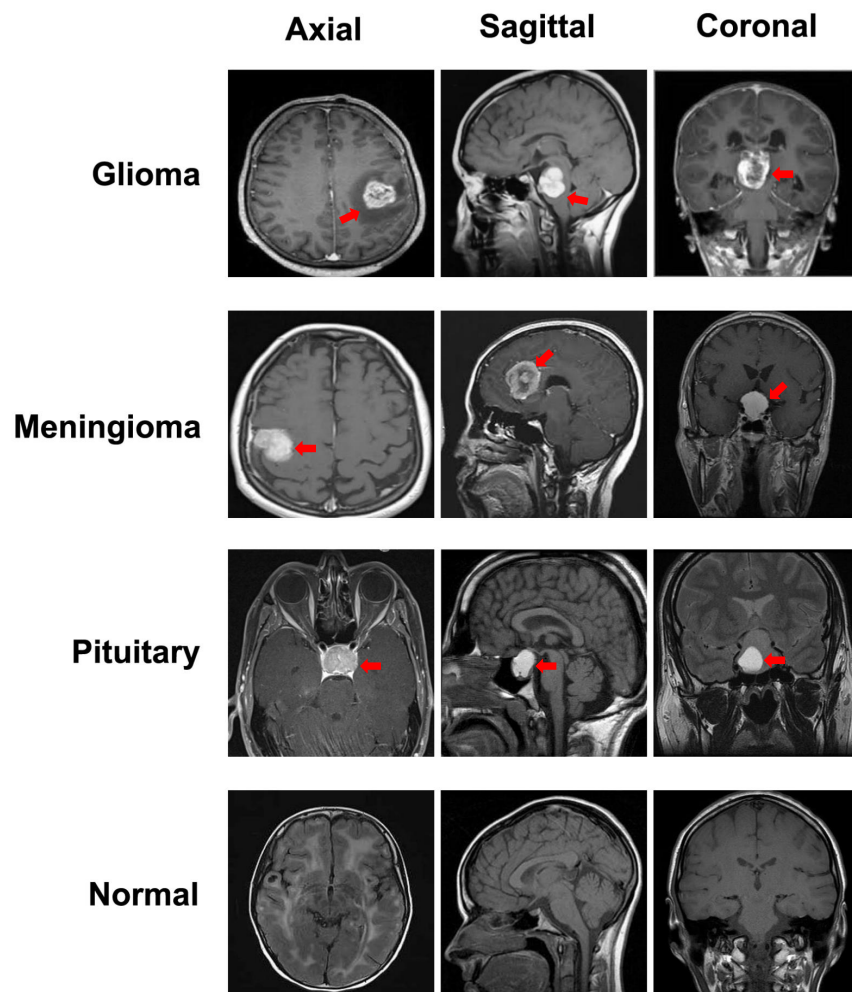
## 2.2 Image Database and Pre-Processing

We consider a Kaggle data set of brain tumor images, as referenced in Bhuvaji et al. (2020). This data set comprises 3,264 MRI images, categorized into four classes: glioma (926 images), meningioma (937 images), pituitary (901 images), and normal (500 images). These images are acquired across three different planes: sagittal, axial and coronal planes. For our study, we randomly split the data set into a training set (2,606 images, 80%) and a test set (658 images, 20%), maintaining the proportion of each class.

The raw images in this data set vary widely in size and resolution, ranging from  $1280 \times 1280$  to  $128 \times 128$  pixels, and include different shapes, such as squares and rectangles. To standardize the data set, we normalize all images into a resolution of  $384 \times 384$  pixels, ensuring a uniform square shape. For the CNN network, we scale the pixel values to the range of  $[0, 1]$ . It is

important to note that no data argumentation is applied to this data set. Figure 2 presents a visual representation of the three types of brain tumors and normal brain tissues, depicted in the three aforementioned planes. Each image distinctly marks the tumor lesions with a red arrow.

Figure 2: Representation of normalized brain tumor MRI images of three brain tumor types and normal brain tissues in three different planes. Red arrows point to the tumor lesions.



## 3 Methodology

### 3.1 Convolutional Neural Networks (CNNs)

Convolutional Neural Networks (ConvNets or CNNs) are state-of-the-art tools for image classification, particularly for massive image data sets. Their effectiveness stems from scalability, high classification accuracy, and efficient optimization (e.g. ImageNet, Russakovsky et al., 2015). They can be further sped up by parallel computation using NVIDIA CUDA GPUs (Li et al., 2014; Cengil et al., 2017; Sultana et al., 2018; Yadav and Jadhav, 2019).

A CNN network model is composed of two major components: feature extraction and classification. In feature extraction, successive convolutional layers and the ReLU activation function work in tandem to extract meaningful features at various dimensions, while pooling layers help in reducing the feature map size. The classification is performed by fully connected dense layers, which utilize the extracted features to estimate class probabilities through a softmax output (see Figure 1). Each neuron in these layers is assigned a weight and a bias, which are learned during the training process. The input to each neuron is a weighted sum, and the output is obtained through a non-linear transformation via activation functions like ReLU.

The convolutional layer involves multiple hyperparameters, including (1) filter, which determines the output space dimensionality and acts as a template to find similarities in the input image; (2) kernel size, such as the height and width of the 2D convolution window; (3) stride, which specifies the convolution strides along the height and width; (4) the padding method, either "valid" (no padding) or "same" (zero padding evenly around the input); (5) activation function, typically ReLU for image classification; (6) kernel regularizer, which applies a regularization function to the kernel weights matrix, such as  $L_1$  (Lasso),  $L_2$  (Ridge), or  $L_1 + L_2$  (Elastic Net).

To stabilize the learning process in each activation layer, a batch normalization layer can be added. This layer normalizes each mini-batch to have a mean close to 0 and a standard deviation close to 1, improving CNN performance and accelerating training (Jung et al., 2019; Amin et al., 2020a; Garbin et al., 2020).

The pooling layer, a critical component of CNNs, reduces computational load by summarizing



features in a region of the feature map from a convolutional layer. This downsizes the feature map and reduces the number of learning parameters. Post-convolution, either max or average pooling, is employed to reduce the input along its spatial dimensions for each channel, with the pooling window shifted by strides along each dimension. The output of the pooling layer feeds into the subsequent convolutional layer, with the final pooling layer being flattened into a feature vector for the classification component, the fully connected neural network layer (Figure 1).

The fully connected (or dense) layer includes a flattened image feature vector as the input layer, several hidden layers with varying neuron sizes, and an output layer with the number of neurons equal to the number of classes, (e.g.,  $K = 4$  in our example). Each neuron is interconnected across adjacent layers. We use ReLU as the activation function between input and hidden layers, softmax to estimate class probabilities, and argmax to predict class labels. The numbers of hidden layers (depth) and neurons are key hyperparameters in the CNN dense layer architecture. Training the network involves computational algorithms such as back-propagation and gradient descent. Different optimization tools and learning rates can affect CNN’s performance in compiling the CNN image classification model. Commonly used optimizers include Adam (Kingma and Ba, 2014) and Adagrad (Duchi et al., 2011).

Given their large number of parameters in the system, CNNs are susceptible to overfitting (Thanapol et al., 2020; Alzubaidi et al., 2021). To mitigate this, techniques such as weight regularization ( $L_1$  and  $L_2$ ) in convolutional layers, dropout layers in dense layers, and early stopping are widely employed. Specifically, random dropout can deactivate some neurons of a layer during training and is shown to be effective in image classifications (Labach et al., 2019; Dileep et al., 2020). Early stopping, which either controls the number of iterations (the epoch length) to avoid overfitting or stops training when no improvement in parameter updates on a validation set, is simple yet effective (Gautam and Singh, 2020; Gaiceanu and Pastravanu, 2021).

Our implementation of CNN for brain tumor MRI image classification was conducted on TensorFlow Core v2.7.0 (Abadi et al., 2015) using Python 3.7 (Van Rossum and Drake, 2009), containerized in Singularity (Kurtzer et al., 2017). This was executed as the University of Arizona High-Performance Computing (HPC) on AMD Zen2 48 core processors with 18GB memory, excluding NVIDIA CUDA GPU acceleration for a fair comparison of computational efficiency

with new methods not utilizing parallel computing technology. Four distinct CNN architectures were implemented for brain tumor MRI image classification, with the results summarized in Table 1.

Table 1: Various Configuration Settings of Four CNN Architectures

CNN	Tumor MRI Image Feature Extraction									Tumor Classification		Model Compilation	
	Convolutional Layers								Pooling	Dense Layer		Optimizer	LR
	Filter	Kernel	Layers	Strides	Padding	L1	L2	BN		Hidden Layers	Dropout		
CNN1	32	3	3	(1, 1)	Valid	0	0	No	Max	(255, )	0	Adam	0.001
CNN2	32	2	4	(2, 2)	Same	0.01	0.001	Yes	Average	(128, )	0.15	Adagrad	0.01
CNN3	64	4	5	(1, 1)	Same	0.001	0.01	Yes	Average	(512, 128)	0.5	Adagrad	0.001
CNN4	128	2	4	(2, 2)	Same	0	0	Yes	Max	(512, 255, 128)	0.25	Adam	0.01

NOTE: The table presents four distinct CNN architectures. BN: Batch Normalization, LR: Model Learning Rate. Batch Normalization is systematically applied after each convolutional layer and just prior to the pooling layer. A dropout layer is incorporated between adjacent layers within the dense network. The configuration of the hidden layer is denoted as  $n$ -tuples, where  $n$  is the number of hidden layers, and each tuple element corresponds to the neuron count in that specific layer. ReLU activation is consistently employed across both the convolutional and dense networks in all configurations. Early stopping is implemented during the compilation of all models.

### 3.2 Bag-of-Features (BoF) Model for Image Classification

Inspired by the Bag-of-Words model, which is extensively utilized in natural language processing and information retrieval, the Bag-of-Features (BoF) approach has been successfully applied to video retrieval (Sivic and Zisserman, 2003) and image classification (Csurka et al., 2004). This technique combines features, represented as  $D$ -dimensional vectors extracted from each normalized training image, into an unordered collection of features (visual words) pool, forming the BoF. This creates a comprehensive representation of the image dataset as a histogram of local descriptors. Owing to the typical vast size of the BoF, stemming from numerous features and training images, a common approach involves clustering these local descriptor features using algorithms such as multi-pass  $k$ -means (Lutz et al., 2018; Sharif et al., 2020). The resulting  $M$ -centroids form a  $\mathbb{R}^{M \times D}$  codebook (vocabulary), offering a compact representation of the image’s local descriptors. If hard vector encoding (VQ) is applied, each visual code has only one non-zero element; in soft-vector encoding (soft-VQ), a small subset of elements will be non-zero (Wang

et al., 2010). Consequently, each image is represented by multiple visual codes, encoded as an  $\mathbb{R}^{M \times S_i}$  matrix, where  $S_i$  denotes the number of descriptors extracted from the  $i$ -th image. This image encoding matrix is then pooled and normalized to generate the final representation of the image features as a  $M$ -vector, equal to the codebook size, for downstream image classification, as illustrated in Figure 1.

### 3.2.1 SIFT-based Image Feature Extraction

The goal of image feature extraction is to capture the most relevant and distinctive characteristics of image patches. Local image descriptors play a pivotal role in tasks such as image classification and object detection in computer vision (Fan et al., 2016). For feature description, we employ the state-of-the-art Scale-Invariant Feature Transform (SIFT) technology Lowe (1999), renowned for its robustness in extracting keypoints under image distortions, rotations, scalings and noise. SIFT is particularly well-suited for extracting features from brain tumor MRI images, which vary in size, angle, and resolution. The SIFT algorithm utilizes cascade filters to compute the Difference of Gaussians (DoG) function progressively on rescaled images, detecting scale-invariant keypoints described by gradient orientation histograms, resulting in a 128-dimensional vector as the scale-invariant local descriptor. The algorithms are detailed in Lowe (2004). For each image, SIFT calculates all the keypoints and corresponding local descriptors, aggregating them to form the image feature representation. This produces a  $\mathbb{R}^{S_i \times D}$  extracted feature matrix, where  $S_i$  is the count of keypoints detected by SIFT for the  $i$ -th image, and  $D$  represents the dimension of the local keypoint descriptor, with  $D = 128$  in our case.

The original brain MRI images in the data set are in JPG format and vary in size. We utilize MATLAB R2020b (The MathWorks, Natick, MA, USA) to uniformly resize each image to a resolution of  $384 \times 384$  pixels, as discussed in 2.2, and then convert them to the PGM format for SIFT input. We run `sift.exe`, downloaded from the open-source VLFeat system at <https://www.vlfeat.org/install-shell.html>, to compute the SIFT features for the  $i$ -th image. The output is a text file, with each row comprising 128 numbers representing a SIFT keypoint descriptor (the initial four numbers, denoting X, Y coordinates, scale, and direction of each keypoint, are removed), and  $S_i$  indicates the number of keypoints detected.

### 3.2.2 Codebook Generation

The Codebook is derived from the BoF feature pool and computed by the multi-pass  $k$ -means algorithm to establish a compact representation of image local descriptors. This is a two-step process outlined as follows.

**(1) BoF Feature Pool** We combine the SIFT descriptors from all the training images to create the BoF feature pool as  $\bigcup_i S_i \times D$ , where  $i$  is the index for each training image,  $D$  is the SIFT descriptor dimension, and specifically,  $D = 128$ . The BoF pool is typically a large matrix, and in our case, the matrix dimensions reach approximately  $8e6 \times 128$ , making it infeasible for the downstream encoding process.

**(2) Create the Codebook** The BoF pool is aggregated to a pre-determined codebook size by multi-pass  $k$ -means (Lutz et al., 2018).  $k$ -means clustering is a well-established method for vector quantization and is widely employed in constructing codebooks or vocabularies (Kanan et al., 2019; Ibrahim et al., 2021). Its primary objective is to partition the set of  $N$ -descriptors into  $M$  clusters, with each descriptor assigned to the cluster with the nearest centroid. These  $M$ -centroids, often referred to as *visual words*, are then assembled to create the  $\mathbb{R}^{M \times D}$  codebook as a compact representation of the image’s local descriptors. The choice between 1-pass  $k$ -means and 2-pass  $k$ -means depends on the pre-defined codebook size and the available computation resources. In our case, we use 2-pass  $k$ -means when  $M > 128$  to ensure efficient computation.

### 3.2.3 Feature Encoding

In the feature encoding phase, the SIFT local descriptor is converted to a “*visual code*”, represented as an  $M$ -vector, by using the aggregated codebook (referred to as vocabulary or dictionary) described above. Common encoding methods include hard vector quantization (VQ) and soft vector quantization (soft-VQ). The key difference is that VQ has only one non-zero element for each visual code, while soft-VQ techniques like Locality-constrained Linear Coding (LLC) may involve a few non-zero elements (Wang et al., 2010). In this paper, we implement both encoding schemes and compare their performance. The details are provided as follows.

### (1) Notations

Let  $\mathbf{X} = [\mathbf{x}_1, \mathbf{x}_2, \dots, \mathbf{x}_N]^T \in \mathbb{R}^{N \times D}$  be the set of local descriptors extracted from images using SIFT, where  $N$  is the number of descriptors, and  $D$  is the dimension of each descriptor. Denote the codebook with  $M$ -centroids as  $\mathbf{B} = [\mathbf{b}_1, \mathbf{b}_2, \dots, \mathbf{b}_M]^T \in \mathbb{R}^{M \times D}$ . During the encoding process, each  $D$ -dimensional descriptor is converted into an  $M$ -dimensional visual code. The final image encoding is represented by a set of these visual codes,  $\mathbf{C} = [\mathbf{c}_1, \mathbf{c}_2, \dots, \mathbf{c}_N]^T \in \mathbb{R}^{N \times M}$ .

### (2) Encoding with VQ

The hard vector quantization (VQ) encoding solves the following constrained least squares optimization problem:

$$\begin{aligned} \min_{\mathbf{C}} \quad & \sum_{i=1}^N \|\mathbf{x}_i - \mathbf{B}^T \mathbf{c}_i\|^2 \\ \text{s.t.} \quad & \|\mathbf{c}_i\|_0 = 1, \quad \|\mathbf{c}_i\|_1 = 1, \quad \mathbf{c}_i \geq 0 \quad \forall i. \end{aligned} \tag{1}$$

The  $L_0$ -norm constraint implies that the number of non-zero elements of  $\mathbf{c}_i$  is 1, while the  $L_1$ -norm and non-negative constraints guarantee that the non-zero element is equal to 1. This constraint-based approach identifies the nearest neighbor of a given descriptor among the  $M$ -centroids using Euclidean distance and assigns a value of 1 in the visual code at the position corresponding to the nearest centroid in the codebook. The time complexity of this process is  $O(M)$ , which is linear in the size of the codebook.

### (3) Encoding with Locality-constrained Linear Coding (LLC)

The soft-VQ encoding can use Lasso-regularized sparse coding with a relaxation of the  $L_0$ -norm constraint (SC-VQ), or add locality constraints using the LLC encoding. Yu et al. (2009) suggests that locality is more essential than sparsity, and Wang et al. (2010) shows that the LLC encoding outperforms SC-VQ and possesses several favorable properties. In particular, the LLC encoding solves the following regularization problem:

$$\begin{aligned} \min_{\mathbf{C}} \quad & \sum_{i=1}^N \|\mathbf{x}_i - \mathbf{B}^T \mathbf{c}_i\|^2 + \lambda \|\mathbf{d}_i \odot \mathbf{c}_i\|^2 \\ \text{s.t.} \quad & \mathbf{1}^T \mathbf{c}_i = 1, \quad \forall i, \end{aligned} \tag{2}$$

where  $\odot$  represents the Hadamard product, and  $\mathbf{d}_i = \exp(\mathbf{dist}(\mathbf{x}_i, \mathbf{B})/\sigma) \in \mathbb{R}^M$  stands for the locality adaptor, which measures the similarity of the input descriptor to each visual word in the codebook based on the Euclidean distance, and  $\lambda$  and  $\sigma$  are hyperparameters to be tuned (Wang et al., 2010). The time complexity of this process is  $O(M^2)$ , which could be computationally inefficient when the number of entries in the codebook is large.

#### (4) Approximate Encoding with Fast LLC

The solution to 2 has few significant values, which in fact performs feature selection of local bases for each descriptor. In practice, only those bases proximate to the given descriptor have non-zero coefficients. Therefore, we can develop a fast approximation of LLC by simply computing the  $K$ -nearest neighbors within the codebook for a given  $i$ -th descriptor. This results in a reduced local base system, denoted as  $\mathbf{B}_i \in \mathbb{R}^{K \times D}$ , where typically  $K < D < M$ . Subsequently, we can solve a much smaller constrained linear system for the visual code:

$$\begin{aligned} \min_{\tilde{\mathbf{C}}} \quad & \sum_{i=1}^N \|\mathbf{x}_i - \mathbf{B}_i^T \tilde{\mathbf{c}}_i\|^2 \\ \text{s.t.} \quad & \mathbf{1}^T \tilde{\mathbf{c}}_i = 1, \quad \forall i \end{aligned} \tag{3}$$

where  $\tilde{\mathbf{C}} = [\tilde{\mathbf{c}}_1, \tilde{\mathbf{c}}_2, \dots, \tilde{\mathbf{c}}_N]^T \in \mathbb{R}^{N \times K}$ . The complete code can be generated by placing the  $K$  elements of  $\tilde{\mathbf{c}}_i$  in the correct positions within  $\mathbf{c}_i$  while setting the remaining  $M - K$  elements to 0. The fast LLC encoding reduces the time complexity to  $O(M + K^2)$ , given that  $K \ll M$ , achieves a linear complexity of  $O(M)$ , which is the same as VQ. However, in practice, VQ is still much faster since LLC encoding typically requires a larger codebook, such as  $M > 1024$ , to obtain optimal results (Wang et al., 2010).

#### 3.2.4 Pooling and Normalization

The image is now represented as a collection of encoding vectors  $\mathbf{C} \in \mathbb{R}^{N \times M}$ , where each descriptor is mapped to a given codebook. These vectors need to be aggregated into a single vector  $\mathbf{q} \in \mathbb{R}^M$  as an input for downstream image classification. This is done by pooling the image encoding features as  $\tilde{\mathbf{q}} \in \mathbb{R}^M$ , which are then normalized to obtain the final image feature representation as the  $M$ -vector  $\mathbf{q}$ . The details are described as follows.

(1) **Pooling** We can do either sum-pooling or max-pooling.

A. Sum pooling:  $\tilde{q}_j = \sum_{i=1}^N \mathbf{C}_{ij}, j = 1, 2, \dots, M$

B. Max pooling:  $\tilde{q}_j = \max_{i=1}^N \mathbf{C}_{ij}, j = 1, 2, \dots, M$

In the case of VQ encoding, sum-pooling computes the histogram of the number of occurrences of each visual code in the image, while max-pooling generates a binary histogram that indicates the presence or absence of each visual code in the image.

## (2) Vector Normalization

Our work shows that various normalization methods for the pooling vector  $\tilde{\mathbf{q}}$  can have a significant impact on downstream image classification. We employ the following three normalization methods:

A. Sum normalization:  $\mathbf{q} = \tilde{\mathbf{q}} / \sum_j \tilde{q}_j, j = 1, 2, \dots, M$

B. L2 normalization:  $\mathbf{q} = \tilde{\mathbf{q}} / \|\tilde{\mathbf{q}}\|_2$

C. Log term frequency weight (LTF) normalization:

We develop this normalization method inspired by the log term frequency weighting within the vector space model of information retrieval theory (Manning et al., 2008). In this approach, we view each element of the pooling vector  $\tilde{q}_j$  as the term frequency within a document containing  $M$  terms. The LTF normalization process is different for pooling from VQ and LLC, as encoding from LLC may include negative values in the pooling vector. For each  $j = 1, 2, \dots, M$ , we obtain the normalized vector  $\mathbf{q}$  from the pooling vector  $\tilde{\mathbf{q}}$  as follows:

(a). Pooling from VQ encoding

$$q_j = \begin{cases} 1 + \log_{10} \tilde{q}_j & \text{if } \tilde{q}_j > 0 \\ 0 & \text{otherwise} \end{cases}$$

(b). Pooling from LLC encoding involves the following steps: (i) set all the negative term frequencies of  $\tilde{q}_j$  to 0; (ii) calculate the minimum positive term frequency, defined as  $\tilde{q}_{min} = \min_j \tilde{q}_j$ , where  $\tilde{q}_j > 0$ ; (iii) perform scaling  $\tilde{\mathbf{q}}^* = \tilde{\mathbf{q}} / \tilde{q}_{min}$ ; (iv) use  $\tilde{\mathbf{q}}^*$  as input and follow the LTF normalization procedure as VQ in (a).

Different combinations of pooling and normalization methods can be used to generate the final

image vector. These choices can lead to significant differences in performance for downstream classification within the wSVMs framework, as elaborated in 4.

### 3.3 Class Probability Estimation via Weighted SVMs

Once we obtain the vector representation of images as  $\mathbf{q} \in \mathbb{R}^M$ , the final step is to perform multiclass classification and probability estimation. Towards this, we employ the weighted Support Vector Machines (wSVMs), which are designed for estimating posterior class probabilities in  $K$ -class problems through ensemble learning (Wu, Zhang and Liu, 2010; Wang, Zhang and Wu, 2019; Zeng and Zhang, 2022). The method is entirely non-parametric, and hence both flexible and robust. Given any input  $\mathbf{x}$ , we estimate its class probabilities  $\hat{p}_j(\mathbf{x})$  for  $j = 1, \dots, K$ , and then construct the classifier by the argmax rule,  $\hat{\phi}(\mathbf{x}) = \arg \max_{1 \leq j \leq K} \hat{p}_j(\mathbf{x})$ , or using the max voting algorithm based on the full pairwise conditional probability table (Zeng and Zhang, 2022).

Various learning schemes have been proposed for multiclass probability estimation within the wSVMs framework. Wu et al. (2010) developed an algorithm that simultaneously learns multiple probability functions, which has nice theoretical properties and empirical performance. However, it involves the exponential time complexity. Wang et al. (2019) proposed the pairwise coupling technique based on divide-and-conquer, reducing the complexity from exponential to polynomial in  $K$ . Recently, Zeng and Zhang (2022) introduced the baseline learning scheme to further lower the computational cost, achieving a linear complexity in  $K$  and making the wSVMs scalable for massive data with a large  $K$ . Furthermore, baseline learning can enhance the pairwise coupling, improving both computation time and estimation accuracy. Finally, the One-vs-All (OVA) learning scheme developed by Zeng and Zhang (2022) exhibits the best empirical performance, although it is not the most computationally efficient. In the following section, we provide a brief review of the wSVMs probability estimation framework.

#### (1) Notations

Denote the entire labeled training set as  $\{(\mathbf{x}_i, y_i), i = 1, \dots, n\}$ , where  $\mathbf{x}_i = (x_{i1}, \dots, x_{ip})^T \in \mathbb{R}^p$ ,  $n$  is the training sample size, and  $p$  is the data dimension. For each class  $j = 1, \dots, K$ , define its training set as  $\mathcal{S}_j = \{(\mathbf{x}_i, y_i) \mid y_i = j; i = 1, \dots, n\}$ . The estimated class probability functions



from the training data are denoted by  $\hat{\mathbf{p}} = \{\hat{p}_1, \dots, \hat{p}_K\}$ , where the magnitude of  $\hat{p}_j$  signifies the confidence level of a data point belonging to class  $j$ . The classification boundary is determined by either the argmax rule,  $\hat{\phi}(\mathbf{x}) = \arg \max_{1 \leq j \leq K} \hat{p}_j(\mathbf{x})$ , or the max voting algorithm (Kallas et al., 2012; Tomar and Agarwal, 2015; Ding et al., 2019) if the pairwise conditional probability table is available.

## (2) Binary wSVMs

In binary classification problems, the class label  $y \in \{+1, -1\}$ . Define the posterior class probabilities as  $p_{+1}(\mathbf{x}) = P(Y = +1 | \mathbf{X} = \mathbf{x})$  and  $p_{-1}(\mathbf{x}) = P(Y = -1 | \mathbf{X} = \mathbf{x})$ , respectively. The binary wSVM solves the following optimization problem:

$$\min_{f \in \mathcal{H}_K} \frac{1}{n} \left[ (1 - \pi) \sum_{y_i=1} L(y_i f(\mathbf{x}_i)) + \pi \sum_{y_i=-1} L(y_i f(\mathbf{x}_i)) \right] + \lambda J(f), \quad (4)$$

where  $L(yf(\mathbf{x})) = (1 - yf(\mathbf{x}))_+ = \max\{0, 1 - yf(\mathbf{x})\}$  is the hinge loss function,  $\mathcal{F}$  is some functional space, the regularization term  $J(f)$  controls model complexity, and the parameter  $\lambda > 0$  balances the bias–variance trade-off (Hastie et al., 2009). For kernel SVMs,  $f$  employs a bivariate Mercer kernel representation  $\mathbf{K}(\cdot, \cdot)$  (Kimeldorf and Wahba, 1971), and the space  $\mathcal{F} = \mathcal{H}_{\mathbf{K}}$  is the reproducing kernel Hilbert space (RKHS, Wahba, 1990) induced by  $\mathbf{K}(\cdot, \cdot)$ . It is known that, for each weight  $\pi$ , the minimizer of the expected weighted hinge loss  $\mathbb{E}_{(\mathbf{X}, Y) \sim P(\mathbf{X}, Y)} \{W(Y)L[Yf(\mathbf{X})]\}$  has the same sign as  $\text{sign}[p_{+1}(\mathbf{X}) - \pi]$  (Lin et al., 2002; Wang et al., 2008). To estimate posterior class probabilities, we first train multiple classifiers  $\hat{f}_{\pi_1}, \dots, \hat{f}_{\pi_M}$  by solving (4) with a series of  $\pi$  values satisfying  $0 < \pi_1 < \dots < \pi_M < 1$ . Theoretically speaking, for each input  $\mathbf{x}$ , the sequence  $\hat{f}_{\pi}(\mathbf{x})$  is non-increasing in  $\pi$ , resulting a unique value  $m^*$  such that  $\pi_{m^*} < p_{+1}(\mathbf{x}) < \pi_{m^*+1}$ . A consistent binary class probability estimator can then be constructed as  $\hat{p}_{+1}(\mathbf{x}) = \frac{1}{2}(\pi_{m^*} + \pi_{m^*+1})$ .

## (3) Multiclass wSVMs

For  $K$ -class problems, where the class label  $y \in \{1, 2, \dots, K\}$  with  $K \geq 3$ , the goal is to estimate class probabilities  $p_j(\mathbf{x}) = P(Y = j | \mathbf{X} = \mathbf{x})$  for  $j = \{1, \dots, K\}$ . When considering any pair of two classes, denoted as  $j$  and  $j'$  with  $1 \leq j \neq j' \leq K$ , we define the pairwise posterior

conditional probability of a data point belonging to class  $j$ , given that it must belong to either class  $j'$  or class  $j$ , as

$$q_{j|(j,j')}(\mathbf{x}) = \frac{P(Y = j|\mathbf{X} = \mathbf{x})}{P(Y = j|\mathbf{X} = \mathbf{x}) + P(Y = j'|\mathbf{X} = \mathbf{x})} = \frac{p_j(\mathbf{x})}{p_j(\mathbf{x}) + p_{j'}(\mathbf{x})}. \quad (5)$$

Wang et al. (2019) proposed the pairwise coupling method, which decomposes the  $K$ -class problem into  $\binom{K}{2}$  binary problems and constructs the class probabilities using all pairwise conditional probability as follows

$$p_j(\mathbf{x}) = \frac{q_{j|(j,k)}(\mathbf{x})/q_{k|(j,k)}(\mathbf{x})}{\sum_{s=1}^K q_{s|(s,k)}(\mathbf{x})/q_{k|(s,k)}(\mathbf{x})}, \quad j = 1, \dots, K; \quad k \neq j. \quad (6)$$

Each pairwise conditional probability is estimated using binary wSVMs. Zeng and Zhang (2022) proposed an algorithm with linear time complexity by selecting a fixed common baseline class  $k^*$  to train  $K - 1$  binary wSVMs problems. Alternatively, one can use the One-vs-All (OVA) approach, which involves training  $K$  binary wSVMs problems for classifying  $j$  vs “not  $j$ ” for  $j = 1, \dots, K$ .

In this work, different codebook sizes and encoding methods may introduce varying levels of complexity in multiclass probability estimation using the wSVMs. We employ the following implementations for the brain tumor MRI image analysis: (i) the pairwise coupling method, denoted as SIBOW-PSVM; (ii) the OVA learning scheme, denoted as SIBOW-ASVM; (iii) the baseline learning scheme, denoted as SIBOW-BSVM, which selects the baseline class either based on the abundance of class data or by considering the aggregated class distance, along with pairwise probability reconstruction as proposed in Zeng and Zhang (2022), denoted as SIBOW-BPSVM. It is observed that the two baseline methods provide similar results.

### 3.4 Model Calibration

To measure the accuracy of multiclass probability estimation across different algorithms, particularly in the absence of true underlying probabilities, we employ model calibration to evaluate the correctness of probability estimation (Guo et al., 2017; Kumar et al., 2018; Minderer et al., 2021). Specifically, to estimate the expected accuracy of class probabilities, we first group the predicted class probabilities  $\hat{p}_{\hat{y}_i}(\tilde{\mathbf{x}}_i)$  into  $M$  interval bins, each with a size of  $\frac{1}{M}$ . Define

$P_m = \{i \mid \hat{p}_{\hat{y}_i}(\tilde{\mathbf{x}}_i) \in (\frac{m-1}{M}, \frac{m}{M}]\}$  for  $m = 1, \dots, M$  and  $i = 1, \dots, \tilde{n}$ . We then calculate the accuracy of  $P_m$  as:

$$\text{acc}(P_m) = \sum_{i \in P_m} I(\hat{y}_i = \tilde{y}_i) / |P_m|,$$

where  $\hat{y}_i$  and  $\tilde{y}_i$  are the predicted and true class labels for the  $i$ -th test sample, and  $I(\cdot)$  is the indicator function. The estimated confidence within bin  $P_m$  is defined as:

$$\text{conf}(P_m) = \sum_{i \in P_m} \hat{p}_{\hat{y}_i}(\tilde{\mathbf{x}}_i) / |P_m|.$$

To visualize model calibration, we employ the *reliability diagram* tool, which graphically represents the expected sample accuracy as a function of confidence. In a perfectly calibrated model, we would have  $\text{acc}(P_m) = \text{conf}(P_m)$  for  $\forall m \in 1, \dots, M$ , resulting in a diagonal line at  $45^\circ$  on the reliability diagram. Any derivations from the ideal scenario indicate miscalibration (Naeini et al., 2015) at some level. The reliability curve for each method is smoothed using Generalized Additive Models (GAM) (Wood et al., 2016) and compared against the  $45^\circ$  line. We quantify the miscalibration in terms of the Expected Calibration Error (ECE), which measures the absolute difference between predictive confidence and accuracy,  $\text{ECE} = \sum_{m=1}^M |P_m| \times |\text{acc}(P_m) - \text{conf}(P_m)| / \tilde{n}$ , where  $\tilde{n}$  is the number of test samples. The smaller the ECE value, the better model calibration.

## 4 Results and Discussion

In this section, we report the results for the brain tumor MRI image data set, as described in 2.2. We compare the proposed SIBOW-SVM with the standard Convolutional Neural Networks (CNNs), in terms of both classification accuracy and probability estimation. The performance is evaluated based on the test set comprising 196 glioma, 185 meningioma, 173 pituitary, and 104 normal images with mixed planes. In addition to the misclassification error, we report the macro (average) precision, recall and F-1 scores by treating all the classes equally.

### 4.1 CNNs

In Table 2, we summarize the results of four CNN network architectures. These CNNs exhibit different levels of complexity, which impact their image classification performance and computa-

tional efficiency. We randomly split the images into training and validation sets of equal sizes, repeated 10 times, and reported the average misclassification rates, macro precision/recall/F-1 scores, and ECE evaluated on the test set, along with standard errors. CNN1 generally gives the best classification and probability estimation performance, CNN4 has the overall worst performance, and CNN3 has the worst time complexity among the models. These results align with the Kaggle code pool with standard CNN implementations.

Table 2: Performance measures on various CNN architectures.

Metrics	CNN1	CNN2	CNN3	CNN4
Time	25.4 (1.8)	19.3 (0.7)	195.5 (4.2)	42.7 (2.8)
TE	22.7 (0.4)	25.4 (0.6)	24.1 (0.7)	29.2 (0.8)
Precision	76.9 (0.4)	74.5 (0.9)	76.4 (0.7)	70.8 (0.8)
Recall	78.3 (0.4)	76.4 (0.7)	75.9 (0.5)	75.4 (1.1)
F1	76.7 (0.4)	73.7 (0.7)	75.1 (0.9)	70.8 (0.9)
ECE	20.2 (0.3)	20.5 (0.3)	20.4 (0.3)	21.0 (0.7)
Epoches	7.7 (0.4)	41.6 (1.3)	19.8 (0.4)	17.4 (1.1)

NOTE: The table shows performance measurements for the four CNN architectures described in Section 3.1. The running time is measured in minutes. The values for TE (misclassification rate), Precision, Recall and F1 (Macro average) are multiplied by 100 for both mean and standard derivation (displayed in parentheses). Training epochs were stopped early if the evaluation loss increased.

## 4.2 SIBOW-SVM Model

In this section, we present the results of the proposed SIBOW-SVM model for image classification, comparing it with the standard CNN architecture. We extracted SIFT features uniformly as a BoF pool and implemented two feature encoding methods: VQ and LLC, as detailed in Section 3.2. These methods require different codebook generation approaches. All encoding features were then pooled and normalized, for example, using “sum pooling” followed by “L2 normalization”, referred to as “sum-L2” pooling. In total, we employed six pooling methods, as outlined in 3.2.4, denoted as (1) “sum-sum”, (2) “sum-L2”, (3) “sum-LTF”, (4) “max-sum”, (5) “max-L2”, and (6) “max-LTF”, as the feature inputs for the wSVMs.

Pooling methods play a critical role in the performance of wSVMs. For VQ encoding, we observe a significant performance difference between two pooling methods: “sum-LTF”, which uses TF-IDF weighting inspired by information retrieval; and “sum-sum”, which employs frequency pooling. Some pooling combinations yielded similar results, and we report the best results.

For kernel wSVMs, hyperparameters were tuned using EGKL, following the procedure in Zeng and Zhang (2022). We randomly split the images into training and tuning sets of equal sizes, repeated 10 times, and reported the average misclassification rates, macro precision/recall/F-1 scores, and ECE evaluated on the test image set, along with standard errors.

#### 4.2.1 VQ Encoding Scheme

VQ encoding generally requires a small codebook size due to its nature of hard vector quantization (Coates and Ng, 2011; Wu and Yu, 2019), making it more computationally efficient for complex problems as we can perform 1-pass  $k$ -means in most cases. In our experiments, we implemented codebooks with sizes of  $M \in \{32, 64, 128\}$ .

**Pooling with “sum-LTF”** Table 3 reports the VQ encoding with the newly developed “sum-LTF” pooling method. We denote schemes with different codebook sizes as **VQ32**, **VQ64**, and **VQ128**. Notably, the VQ64 encoding with wSVMs enhanced by pairwise coupling and baseline learning (BP1-SVM and BP2-SVM) yielded the best performance, showing a 12% increase in classification accuracy, a 14% increase in macro-precision, a 12% increase in macro-recall, and a 15% increase in macro-F1 score. For multiclass probability estimation, it resulted in a 57% reduction in ECE (model calibration error) and a 63% reduction in computation time compared to the standard convolutional neural network’s best performer CNN1. The OVA-SVM (A-SVM) consistently provided the best estimation yet comparable performance as the baseline learning across various encoding schemes, but with more computation times. The codebook size was critical, as the performance decreased when  $M$  changed, as shown in the VQ32 and VQ128 schemes.

**Pooling with “sum-sum”** Table 4 reports the results for VQ encoding with “sum-sum” as frequency pooling. We denote schemes with different codebook sizes as **PF32**, **PF64**, and **PF128**. It was observed that, with the same encoding vector, changing the pooling method from “sum-LTF” to “sum-sum” led to a significant decrease in performance. PF128 was the best performer, showing a 15% decrease in classification accuracy, a 17% decrease in macro F1, and a 94% increase in ECE. It provided the optimal results only with the newly developed “sum-LTF” pooling.

#### 4.2.2 LLC Encoding Scheme

Compared to VQ, LLC encoding requires larger codebook sizes for optimal performance (Wang et al., 2010). In our experiments, we implemented codebooks with sizes of  $M \in \{2048, 4096, 8192\}$ . The performance for  $M > 2^{14}$  drastically deteriorated in both computational efficiency and performance. Since  $D \ll M$ , we implemented the fast approximate LLC encoding described in Section 3.2.3. We chose  $K = 5$ , following Wang et al. (2010). We evaluated 6 pooling methods.

Table 5 reports the result for LLC encoding with “max-L2” (the same result as “sum-L2”) pooling, which consistently gave the best performance. We denote the schemes with different codebook sizes as **LLC2048**, **LLC4096**, and **LLC8192**. Table t suggests that LLC8192 gave the best result, surpassing the standard CNN and VQ32, but at the cost of more than a tenfold increase in computation time. LLC encoding performed better with higher-resolution images, as it could extract more locality information compared to VQ.

Table 3: Performance measure of VQ encoding with sum-LTF pooling

<b>VQ32</b>	<b>B1-SVM</b>	<b>BP1-SVM</b>	<b>B2-SVM</b>	<b>BP2-SVM</b>	<b>A-SVM</b>	<b>P-SVM</b>
Time	13.1 (0.2)	13.1 (0.2)	11.9 (0.8)	11.9 (0.8)	143.1 (3.2)	22.4 (0.2)
TE1	19.1 (0.4)	18.9 (0.3)	19.1 (0.4)	19.0 (0.4)	18.3 (0.3)	19.0 (0.4)
TE2	NA (NA)	18.7 (0.3)	NA (NA)	18.8 (0.4)	NA (NA)	18.8 (0.3)
Precision	81.8 (0.2)	81.9 (0.2)	81.5 (0.2)	81.8 (0.3)	82.2 (0.4)	81.7 (0.4)
Recall	81.4 (0.3)	81.6 (0.2)	81.5 (0.3)	81.6 (0.3)	82.8 (0.4)	81.6 (0.4)
F1	81.2 (0.3)	81.4 (0.2)	81.2 (0.3)	81.3 (0.3)	82.2 (0.4)	81.3 (0.4)
ECE	12.4 (0.4)	12.2 (0.3)	12.5 (0.4)	12.3 (0.3)	11.8 (0.2)	12.3 (0.5)
$k^*$	2	2	4	4	NA (NA)	NA (NA)
<b>VQ64</b>	<b>B1-SVM</b>	<b>BP1-SVM</b>	<b>B2-SVM</b>	<b>BP2-SVM</b>	<b>A-SVM</b>	<b>P-SVM</b>
Time	11.0 (0.1)	11.0 (0.1)	9.5 (0.7)	9.5 (0.7)	107.6 (2.0)	19.4 (0.2)
TE1	14.3 (0.2)	14.3 (0.2)	14.4 (0.2)	14.3 (0.2)	13.7 (0.2)	14.3 (0.2)
TE2	NA (NA)	13.8 (0.2)	NA (NA)	13.9 (0.2)	NA (NA)	13.9 (0.2)
Precision	87.3 (0.2)	87.6 (0.1)	87.1 (0.2)	87.3 (0.2)	88.3 (0.2)	87.3 (0.1)
Recall	86.9 (0.2)	87.2 (0.2)	86.7 (0.1)	86.9 (0.1)	87.7 (0.2)	86.8 (0.2)
F1	87.2 (0.2)	87.5 (0.2)	87.1 (0.2)	87.2 (0.2)	88.0 (0.2)	87.1 (0.2)
ECE	9.3 (0.3)	8.9 (0.3)	9.4 (0.3)	9.0 (0.2)	8.7 (0.3)	9.3 (0.2)
$k^*$	2	2	2	2	NA (NA)	NA (NA)
<b>VQ128</b>	<b>B1-SVM</b>	<b>BP1-SVM</b>	<b>B2-SVM</b>	<b>BP2-SVM</b>	<b>A-SVM</b>	<b>P-SVM</b>
Time	10.7 (0.1)	10.7 (0.1)	8.5 (0.8)	8.5 (0.8)	97.7 (1.2)	18.5 (0.0)
TE1	29.1 (0.4)	29.1 (0.4)	29.2 (0.4)	29.2 (0.4)	28.2 (0.3)	29.1 (0.5)
TE2	NA (NA)	29.1 (0.4)	NA (NA)	29.1 (0.5)	NA (NA)	29.1 (0.4)
Precision	67.2 (0.4)	67.5 (0.3)	67.1 (0.2)	67.4 (0.2)	68.3 (0.5)	67.3 (0.4)
Recall	83.3 (0.3)	83.5 (0.2)	83.2 (0.2)	83.4 (0.2)	84.2 (0.6)	83.4 (0.4)
F1	68.8 (0.6)	69.1 (0.6)	68.8 (0.6)	69.0 (0.6)	70.1 (0.5)	69.0 (0.5)
ECE	14.6 (0.4)	14.4 (0.3)	14.5 (0.4)	14.3 (0.2)	14.0 (0.5)	14.4 (0.5)
$k^*$	2	2	3	3	NA (NA)	NA (NA)

NOTE: The table presents performance measurements for VQ encoding with sum-LTF pooling using three code-book sizes. The running time is measured in minutes. TE1 (misclassification rate based on max probability), TE2 (misclassification rate based on max voting), macro precision, macro recall, macro F1, and ECE are multiplied by 100 for both mean and standard derivation (in parentheses). The optimal baseline class  $k^*$  for the baseline methods is calculated using the statistical mode. Similar explanations apply to the results for other encoding methods.

Table 4: Performance measure of VQ encoding with sum-sum pooling

<b>PF32</b>	<b>B1-SVM</b>	<b>BP1-SVM</b>	<b>B2-SVM</b>	<b>BP2-SVM</b>	<b>A-SVM</b>	<b>P-SVM</b>
Time	17.6 (0.3)	17.6 (0.3)	16.5 (0.9)	16.5 (0.9)	247.0 (4.6)	29.9 (0.8)
TE1	30.2 (0.3)	30.2 (0.3)	30.3 (0.3)	30.3 (0.3)	29.5 (0.2)	30.0 (0.3)
TE2	NA (NA)	29.8 (0.3)	NA (NA)	29.9 (0.3)	NA (NA)	29.8 (0.3)
Precision	69.0 (0.3)	69.3 (0.4)	68.8 (0.3)	69.1 (0.3)	69.8 (0.2)	69.1 (0.3)
Recall	70.6 (0.2)	70.9 (0.2)	70.5 (0.3)	70.7 (0.4)	71.9 (0.3)	70.8 (0.3)
F1	69.3 (0.4)	69.6 (0.4)	69.2 (0.3)	69.5 (0.3)	70.5 (0.2)	69.5 (0.3)
ECE	16.7 (0.2)	16.4 (0.2)	16.6 (0.2)	16.3 (0.2)	16.1 (0.3)	16.3 (0.3)
$k^*$	2	2	4	4	NA (NA)	NA (NA)
<b>PF64</b>	<b>B1-SVM</b>	<b>BP1-SVM</b>	<b>B2-SVM</b>	<b>BP2-SVM</b>	<b>A-SVM</b>	<b>P-SVM</b>
Time	17.2 (0.5)	17.2 (0.5)	17.3 (0.5)	17.3 (0.5)	235.8 (6.0)	29.7 (0.7)
TE1	28.2 (0.1)	28.1 (0.2)	28.1 (0.1)	28.0 (0.1)	27.4 (0.2)	28.1 (0.2)
TE2	NA (NA)	27.8 (0.1)	NA (NA)	27.8 (0.1)	NA (NA)	28.0 (0.2)
Precision	69.6 (0.5)	69.9 (0.4)	69.9 (0.4)	71.1 (0.4)	71.6 (0.3)	71.0 (0.2)
Recall	72.7 (0.3)	72.8 (0.4)	72.6 (0.3)	72.8 (0.2)	73.4 (0.3)	72.7 (0.2)
F1	71.3 (0.5)	71.4 (0.4)	71.5 (0.4)	71.6 (0.4)	72.4 (0.3)	71.5 (0.2)
ECE	16.7 (0.3)	16.4 (0.3)	16.9 (0.3)	16.6 (0.3)	16.0 (0.2)	16.6 (0.2)
$k^*$	1	1	2	2	NA (NA)	NA (NA)
<b>PF128</b>	<b>B1-SVM</b>	<b>BP1-SVM</b>	<b>B2-SVM</b>	<b>BP2-SVM</b>	<b>A-SVM</b>	<b>P-SVM</b>
Time	16.3 (0.3)	16.3 (0.3)	14.6 (1.0)	14.6 (1.0)	228.6 (5.7)	28.0 (0.4)
TE1	26.7 (0.2)	26.7 (0.2)	26.7 (0.2)	26.6 (0.2)	25.9 (0.2)	26.6 (0.1)
TE2	NA (NA)	26.1 (0.2)	NA (NA)	26.1 (0.2)	NA (NA)	26.4 (0.2)
Precision	72.3 (0.3)	72.6 (0.4)	72.2 (0.4)	72.4 (0.4)	72.6 (0.2)	72.4 (0.2)
Recall	74.5 (0.4)	74.8 (0.4)	74.3 (0.4)	74.6 (0.3)	75.4 (0.2)	74.7 (0.2)
F1	73.0 (0.4)	73.1 (0.4)	72.8 (0.4)	72.9 (0.4)	73.6 (0.2)	73.0 (0.2)
ECE	17.4 (0.2)	17.1 (0.2)	17.6 (0.4)	17.2 (0.4)	16.8 (0.3)	17.3 (0.4)
$k^*$	2	2	1	1	NA (NA)	NA (NA)



Table 5: Performance measure of LLC encoding with max-L2 pooling

<b>LLC2048</b>	<b>B1-SVM</b>	<b>BP1-SVM</b>	<b>B2-SVM</b>	<b>BP2-SVM</b>	<b>A-SVM</b>	<b>P-SVM</b>
Time	34.8 (2.4)	34.8 (2.4)	34.3 (2.3)	34.3 (2.3)	252.9 (9.6)	60.8 (4.0)
TE1	33.5 (0.6)	33.5 (0.6)	33.7 (0.6)	33.7 (0.6)	32.7 (0.6)	33.6 (0.6)
TE2	NA (NA)	33.2 (0.6)	NA (NA)	33.3 (0.7)	NA (NA)	33.3 (0.6)
Precision	66.8 (0.7)	67.1 (0.7)	66.4 (0.6)	66.8 (0.6)	67.3 (0.5)	66.9 (0.5)
Recall	68.8 (0.4)	69.0 (0.4)	68.6 (0.5)	68.9 (0.5)	69.1 (0.6)	69.0 (0.6)
F1	67.3 (0.6)	67.6 (0.6)	67.1 (0.5)	67.4 (0.5)	68.1 (0.5)	67.5 (0.6)
ECE	17.6 (0.4)	17.4 (0.3)	17.6 (0.2)	17.4 (0.3)	17.2 (0.4)	17.5 (0.3)
$k^*$	2	2	1	1	NA (NA)	NA (NA)
<b>LLC4096</b>	<b>B1-SVM</b>	<b>BP1-SVM</b>	<b>B2-SVM</b>	<b>BP2-SVM</b>	<b>A-SVM</b>	<b>P-SVM</b>
Time	52.7 (0.8)	52.7 (0.8)	53.3 (0.8)	53.3 (0.8)	564.4 (33.4)	94.4 (1.3)
TE1	24.5 (0.4)	24.4 (0.4)	24.7 (0.4)	24.6 (0.4)	23.9 (0.4)	24.3 (0.4)
TE2	NA (NA)	24.0 (0.5)	NA (NA)	24.2 (0.5)	NA (NA)	24.3 (0.4)
Precision	75.1 (0.6)	75.5 (0.5)	75.0 (0.5)	75.3 (0.5)	75.8 (0.5)	75.3 (0.4)
Recall	77.3 (0.6)	77.7 (0.5)	77.2 (0.5)	77.4 (0.4)	77.8 (0.5)	77.5 (0.4)
F1	75.7 (0.6)	76.1 (0.6)	75.5 (0.4)	75.8 (0.4)	76.6 (0.5)	75.9 (0.4)
ECE	14.2 (0.4)	14.0 (0.4)	14.7 (0.2)	14.4 (0.2)	13.9 (0.3)	14.4 (0.4)
$k^*$	2	2	1	1	NA (NA)	NA (NA)
<b>LLC8192</b>	<b>B1-SVM</b>	<b>BP1-SVM</b>	<b>B2-SVM</b>	<b>BP2-SVM</b>	<b>A-SVM</b>	<b>P-SVM</b>
Time	112.4 (4.6)	112.4 (4.6)	93.7 (7.5)	93.8 (7.5)	618.6 (13.0)	200.1 (8.9)
TE1	18.2 (0.2)	18.2 (0.2)	18.2 (0.2)	18.1 (0.2)	18.0 (0.2)	18.1 (0.2)
TE2	NA (NA)	18.1 (0.2)	NA (NA)	18.0 (0.2)	NA (NA)	18.1 (0.2)
Precision	81.1 (0.6)	81.3 (0.3)	81.2 (0.2)	81.5 (0.3)	82.5 (0.2)	81.3 (0.3)
Recall	83.7 (0.4)	83.8 (0.4)	83.7 (0.3)	84.0 (0.3)	84.3 (0.3)	83.9 (0.2)
F1	81.8 (0.4)	82.0 (0.4)	81.9 (0.3)	82.2 (0.3)	82.6 (0.3)	81.9 (0.2)
ECE	12.4 (0.3)	12.0 (0.4)	12.6 (0.4)	12.3 (0.4)	11.6 (0.2)	12.3 (0.4)
$k^*$	2	2	1	1	NA (NA)	NA (NA)

### 4.3 Discussion

In this article, we introduced the SIBOW-SVM model, which incorporates two encoding schemes, VQ and LLC. These novel methods have demonstrated significant improvements over standard CNN architectures in the context of brain tumor MRI image classification and probability estimation, particularly when paired with appropriate encoding and pooling methods for the final image feature representation.

We conducted a comprehensive comparison between the two top-performing two SIBOW-SVM model schemes, VQ64 and LLC8192, and the standard CNN architecture to evaluate multiclass probability estimation and classification. Figure 3 displays a heat map of the probability estimates for the four tumor classes, showcasing that our new methods yield superior class probability grouping compared to CNN. In Figure 4, the reliability diagram illustrates the quality of class probability estimation. The SIBOW-SVM consistently exhibits better model calibration by closely adhering to the diagonal line at a  $45^\circ$ , outperforming the four CNNs. In particular, the VQ64 scheme achieves nearly perfect calibration across all wSVMs methods.

Figure 5 presents multiclass receiver operating characteristic (ROC) curves and the confusion star as a visual representation of the confusion matrix (Luque et al., 2022). Our methods excel in multiclass classification, achieving higher multiclass AUC scores defined by Hand and Till (2001) and smaller polar lengths as an error measure for the confusion matrix. Our SIBOW-SVM models consistently exhibit robust and superior performance compared to standard CNNs, with VQ64 consistently outperforming all other methods. These results underscore the promise of VQ64 for challenging image classification tasks.

In the literature, it has been demonstrated that soft-VQ encoding methods such as LLC offer better performance in image classification tasks (Wang et al., 2010; Agustsson et al., 2017), due to their ability to capture more locality information. However, LLC typically requires a large codebook with high-dimensional final image features, which can slow down computations. Our findings suggest that, VQ encoding, when paired with appropriate encoding and pooling methods, can achieve better performance within the wSVMs framework for probability estimation while maintaining reduced computational complexity. Furthermore, the downstream wSVMs framework can be significantly accelerated through parallel computing, leveraging its divide-

and-conquer nature, making it a competitive alternative to CNNs with NVIDIA CUDA GPU acceleration.

Figure 3: This figure plots the average multiclass probability estimation heat map for VQ64 SIBOW-BPSVM, LLC8192 SIBOW-BPSVM, and CNN1, based on 10 simulations.

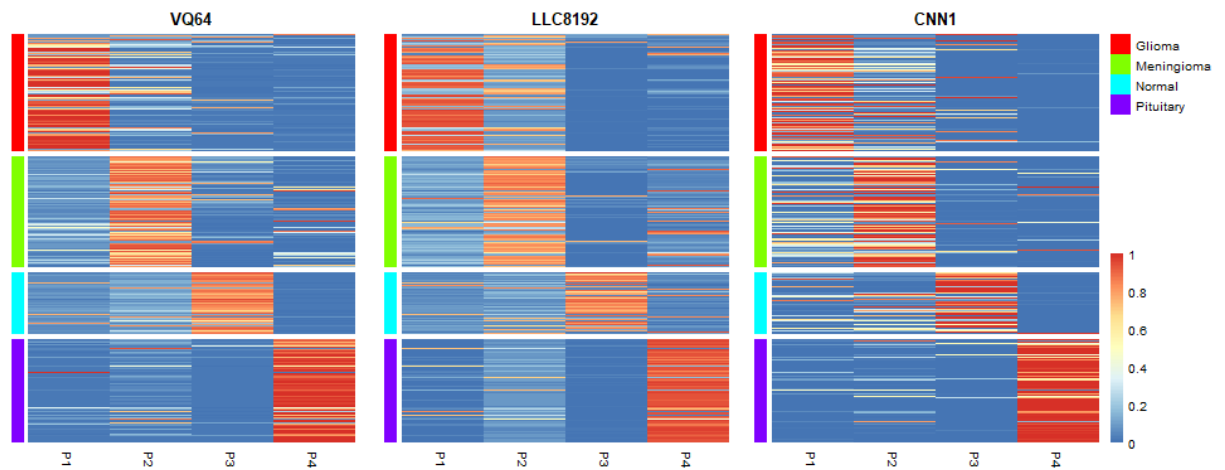


Figure 4: This figure plots the reliability diagrams for VQ64, LLC8194 and 4 CNN architectures. The reliability curves have been smoothed using GAM. Different colors represent different methods. A close proximity with the diagonal line indicates accurate model calibration.

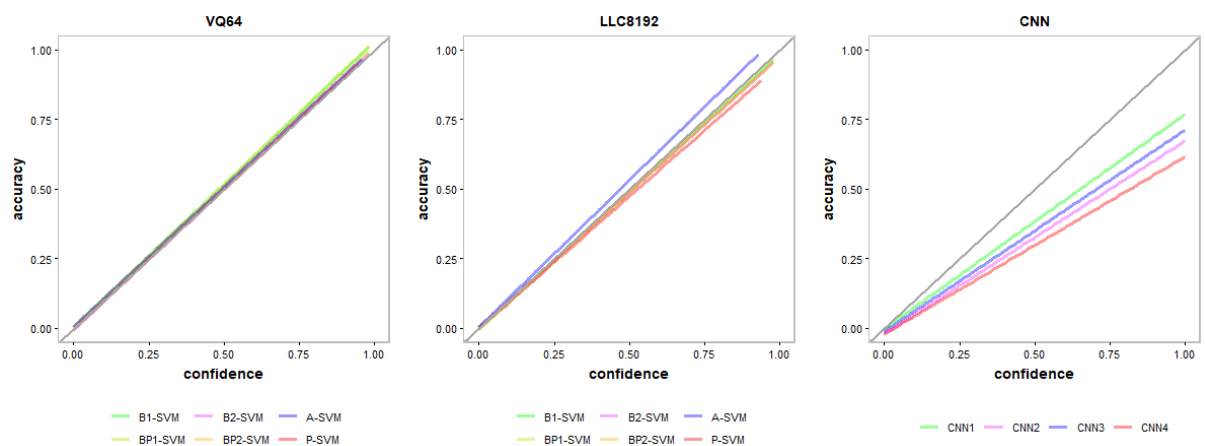
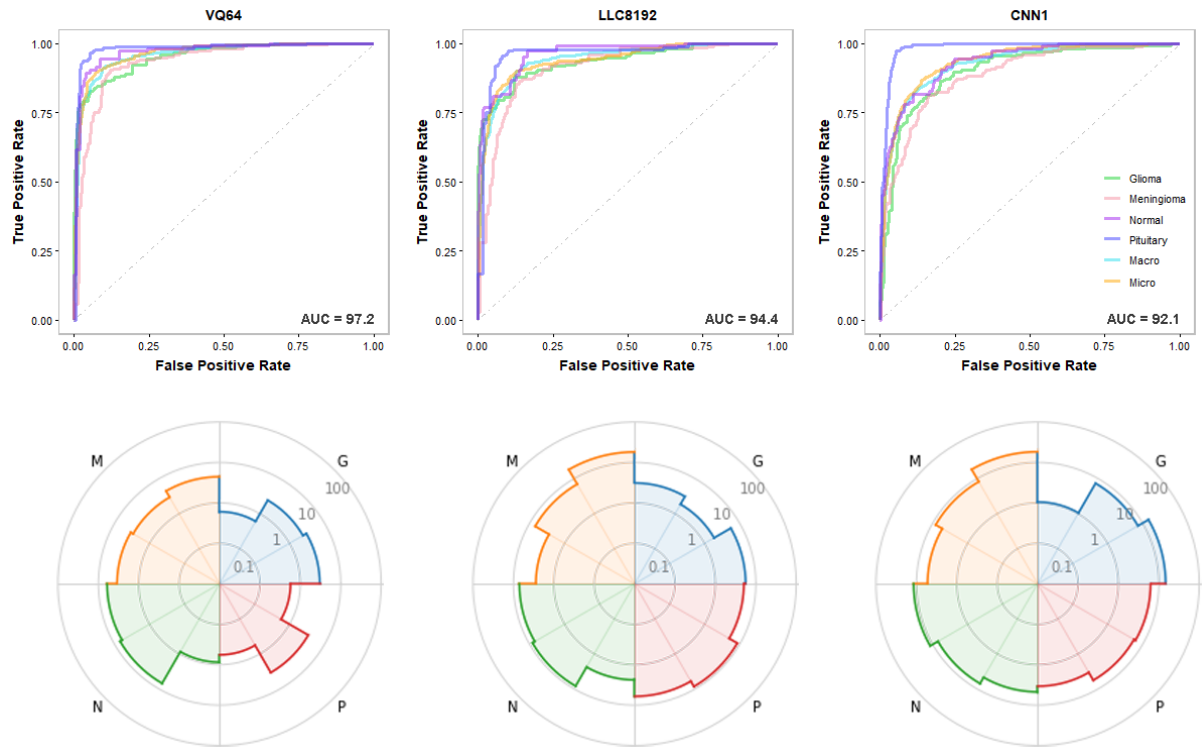


Figure 5: This figure plots the multiclass ROC curves and confusion stars for VQ64 SIBOW-BPSVM, LLC8192 SIBOW-BPSVM, and CNN1. A higher multiclass AUC value indicates a better classifier. A smaller area of the confusion star suggests a lower error in the multiclass confusion matrix.



## 5 Concluding Remarks

The proposed SIBOW-SVM framework shows promise as a method for image classification and confidence measurement of predictions. The wSVMs with baseline learning exhibit overall high accuracy and computational efficiency, making it a favorable approach for multiclass probability estimation in image classifications. The SIBOW-SVM, when coupled with appropriate encoding and pooling methods, consistently provides robust and improved class probability estimation and image classification compared to standard CNNs.

For further work, we plan to enhance the SIBOW-SVM by incorporating sparse learning capabilities. In practice, images with high noise and low resolution are common, leading to the extraction of noisy features by the SIFT algorithm. The current SIBOW-SVM only works effectively with dense features, and its performance may significantly deteriorate when dealing with sparse image features. to address this challenge, we may introduce  $L_1$ -norm regularization to the SIBOW-wSVMs, enabling automatic feature selection and image classification in the presence of numerous noise features.

## References

- ABADI, M., AGARWAL, A., BARHAM, P., BREVDO, E., CHEN, Z., CITRO, C., CORRADO, G. S., DAVIS, A., DEAN, J., DEVIN, M., GHEMAWAT, S., GOODFELLOW, I., HARP, A., IRVING, G., ISARD, M., JIA, Y., JOZEFOWICZ, R., KAISER, L., KUDLUR, M., LEVENBERG, J., MANÉ, D., MONGA, R., MOORE, S., MURRAY, D., OLAH, C., SCHUSTER, M., SHLENS, J., STEINER, B., SUTSKEVER, I., TALWAR, K., TUCKER, P., VANHOUCHE, V., VASUDEVAN, V., VIÉGAS, F., VINYALS, O., WARDEN, P., WATTENBERG, M., WICKE, M., YU, Y. and ZHENG, X. (2015). TensorFlow: Large-scale machine learning on heterogeneous systems. Software available from tensorflow.org, URL <https://www.tensorflow.org/>.
- AFSHAR, P., PLATANIOTIS, K. N. and MOHAMMADI, A. (2019). Capsule networks for brain tumor classification based on mri images and coarse tumor boundaries. *ICASSP 2019 - 2019 IEEE International Conference on Acoustics, Speech and Signal Processing (ICASSP)* 1368–1372.
- AGUSTSSON, E., MENTZER, F., TSCHANNEN, M., CAVIGELLI, L., TIMOFTE, R., BENINI, L. and GOOL, L. V. (2017). Soft-to-hard vector quantization for end-to-end learning compressible representations. In *Advances in Neural Information Processing Systems*, vol. 30. Curran Associates, Inc. URL <https://proceedings.neurips.cc/paper/2017/file/86b122d4358357d834a87ce618a55de0-Paper.pdf>.
- ALZUBAIDI, L., ZHANG, J., HUMAIDI, A. J., AL-DUJAILI, A., DUAN, Y., AL-SHAMMA, O.,

- SANTAMARÍA, J., FADHEL, M. A., AL-AMIDIE, M. and FARHAN, L. (2021). Review of deep learning: concepts, CNN architectures, challenges, applications, future directions. *Journal of Big Data*, **8** 53. URL <https://doi.org/10.1186/s40537-021-00444-8>.
- AMIN, J., SHARIF, M., ANJUM, M. A., RAZA, M. and BUKHARI, S. A. C. (2020a). Convolutional neural network with batch normalization for glioma and stroke lesion detection using mri. *Cognitive Systems Research*, **59** 304–311. URL <https://www.sciencedirect.com/science/article/pii/S1389041719305029>.
- AMIN, J., SHARIF, M., YASMIN, M. and FERNANDES, S. L. (2020b). A distinctive approach in brain tumor detection and classification using MRI. *Pattern Recognition Letters*, **139** 118–127. URL <https://www.sciencedirect.com/science/article/pii/S016786551730404X>.
- AYADI, W., ELHAMZI, W., CHARFI, I. and ATRI, M. (2021). Deep CNN for brain tumor classification. *Neural Processing Letters*, **53** 671–700. URL <https://doi.org/10.1007/s11063-020-10398-2>.
- BARANWAL, S. K., JAISWAL, K., VAIBHAV, K., KUMAR, A. and SRIKANTASWAMY, R. (2020). Performance analysis of brain tumour image classification using CNN and SVM. In *2020 Second International Conference on Inventive Research in Computing Applications (ICIRCA)*. IEEE, Coimbatore, India, 537–542. URL <https://ieeexplore.ieee.org/document/9183023/>.
- BHUVAJI, S., KADAM, A., BHUMKAR, P., DEDGE, S. and KANCHAN, S. (2020). Brain tumor classification (MRI). URL <https://www.kaggle.com/dsv/1183165>.
- BREIMAN, L., H. FRIEDMAN, J., A. OLSHEN, R. and J. STONE, C. (1984). *Classification and regression trees*. Wadsworth Publishing Company, Belmont, California, U.S.A.
- BURGER, P. C. and SCHEITHAUER, B. W. (1994). *Tumors of the Central Nervous System*. Armed Forces Institute of Pathology.
- CENGIL, E., ÇINAR, A. and GÜLER, Z. (2017). A gpu-based convolutional neural network approach for image classification. In *2017 International Artificial Intelligence and Data Processing Symposium (IDAP)*. 1–6.

- CHAMASEMANI, F. F. and SINGH, Y. P. (2011). Multi-class support vector machine (SVM) classifiers – an application in hypothyroid detection and classification. In *2011 Sixth International Conference on Bio-Inspired Computing: Theories and Applications*. 351–356.
- CHEN, T. and GUESTRIN, C. (2016). XGBoost: A scalable tree boosting system. In *Proceedings of the 22nd ACM SIGKDD International Conference on Knowledge Discovery and Data Mining*. KDD '16, ACM, New York, NY, USA, 785–794. URL <http://doi.acm.org/10.1145/2939672.2939785>.
- COATES, A. and NG, A. Y. (2011). The importance of encoding versus training with sparse coding and vector quantization. In *ICML*. 921–928.
- CSURKA, G., DANCE, C. R., FAN, L., WILLAMOWSKI, J. and BRAY, C. (2004). Visual categorization with bags of keypoints. In *In Workshop on Statistical Learning in Computer Vision, ECCV*. 1–22.
- CURRIE, G., HAWK, K. E., ROHREN, E., VIAL, A. and KLEIN, R. (2019). Machine learning and deep learning in medical imaging: Intelligent imaging. *Journal of Medical Imaging and Radiation Sciences*, **50** 477–487. URL <https://www.sciencedirect.com/science/article/pii/S1939865419305041>.
- DEANGELIS, L. M. (2001). Brain tumors. *The New England Journal of Medicine*, **344** 114–123.
- DILEEP, P., DAS, D. and BORA, P. K. (2020). Dense layer dropout based cnn architecture for automatic modulation classification. In *2020 National Conference on Communications (NCC)*. 1–5.
- DING, S., ZHAO, X., ZHANG, J., ZHANG, X. and XUE, Y. (2019). A review on multi-class TWSVM. *Artificial Intelligence Review*, **52** 775–801. URL <http://link.springer.com/10.1007/s10462-017-9586-y>.
- DUCHI, J., HAZAN, E. and SINGER, Y. (2011). Adaptive subgradient methods for online learning and stochastic optimization. *Journal of Machine Learning Research*, **12** 2121–2159.

- FAN, B., WANG, Z. and WU, F. (2016). *Local Image Descriptor: Modern Approaches*. 1st ed. Springer Publishing Company, Incorporated.
- FEBRIANTO, D. C., SOESANTI, I. and NUGROHO, H. A. (2020). Convolutional neural network for brain tumor detection. *IOP Conference Series: Materials Science and Engineering*, **771** 012031. URL <https://doi.org/10.1088/1757-899x/771/1/012031>.
- GAICEANU, T. and PASTRAVANU, O. (2021). On CNN applied to speech-to-text – comparative analysis of different gradient based optimizers. In *2021 IEEE 15th International Symposium on Applied Computational Intelligence and Informatics (SACI)*. 000085–000090.
- GARBIN, C., ZHU, X. and MARQUES, O. (2020). Dropout vs. batch normalization: an empirical study of their impact to deep learning. *Multimedia Tools and Applications*, **79** 12777–12815. URL <https://doi.org/10.1007/s11042-019-08453-9>.
- GAUTAM, A. and SINGH, V. (2020). CNN-VSR: A deep learning architecture with validation-based stopping rule for time series classification. *Applied Artificial Intelligence*, **34** 101–124. <https://doi.org/10.1080/08839514.2020.1713454>, URL <https://doi.org/10.1080/08839514.2020.1713454>.
- GAVALI, P. and BANU, J. S. (2019). Chapter 6 - Deep Convolutional Neural Network for Image Classification on CUDA Platform. In *Deep Learning and Parallel Computing Environment for Bioengineering Systems* (A. K. Sangaiah, ed.). Academic Press, 99–122. URL <https://www.sciencedirect.com/science/article/pii/B9780128167182000130>.
- GIGER, M. L. (2018). Machine learning in medical imaging. *Journal of the American College of Radiology*, **15** 512–520. URL <https://www.sciencedirect.com/science/article/pii/S1546144017316733>.
- GUO, C., PLEISS, G., SUN, Y. and WEINBERGER, K. Q. (2017). On calibration of modern neural networks. In *Proceedings of the 34 th International Conference on Machine Learning*. Sydney, Australia. ArXiv: 1706.04599, URL <http://arxiv.org/abs/1706.04599>.



- HAND, D. J. and TILL, R. J. (2001). A simple generalisation of the area under the ROC curve for multiple class classification problems. *Machine Learning*, **45** 171–186. URL <https://doi.org/10.1023/A:1010920819831>.
- HASHEMZEHI, R., MAHDAVI, S. J. S., KHEIRABADI, M. and KAMEL, S. R. (2020). Detection of brain tumors from MRI images base on deep learning using hybrid model CNN and NADE. *Biocybernetics and Biomedical Engineering*, **40** 1225–1232. URL <https://www.sciencedirect.com/science/article/pii/S0208521620300784>.
- HASTIE, T., TIBSHIRANI, R. and FRIEDMAN, J. (2009). *The elements of statistical learning: data mining, inference and prediction*. 2nd ed. Springer. URL <http://www-stat.stanford.edu/~tibs/ElemStatLearn/>.
- HIBA, C., HAMID, Z. and OMAR, A. (2016). Bag of features model using the new approaches: A comprehensive study. *International Journal of Advanced Computer Science and Applications*, **7**. URL <http://dx.doi.org/10.14569/IJACSA.2016.070132>.
- HISHII, M., MATSUMOTO, T. and ARAI, H. (2019). Diagnosis and treatment of early-stage glioblastoma. *Asian Journal of Neurosurgery*, **14** 589. URL <http://www.asianjns.org/text.asp?2019/14/2/589/252944>.
- HO, T. K. (1995). Random decision forests. In *Proceedings of 3rd international conference on document analysis and recognition*, vol. 1. IEEE, 278–282.
- IBRAHIM, R. K., ZEEBAREE, S. R. M., JACKSI, K., SADEEQ, M. A. M., SHUKUR, H. M. and ALKHAYYAT, A. (2021). Design a clustering document based semantic similarity system using tfidf and k-mean. In *2021 4th International Iraqi Conference on Engineering Technology and Their Applications (IICETA)*. 87–93.
- IQBAL, S., GHANI, M. U., SABA, T. and REHMAN, A. (2018). Brain tumor segmentation in multi-spectral mri using convolutional neural networks (CNN). *Microscopy Research and Technique*, **81** 419–427. URL <https://analyticalsciencejournals.onlinelibrary.wiley.com/doi/abs/10.1002/jemt.22994>.

- JOHNSON, D. R., GUERIN, J. B., GIANNINI, C., MORRIS, J. M., ECKEL, L. J. and KAUFMANN, T. J. (2017). 2016 updates to the who brain tumor classification system: What the radiologist needs to know. *RadioGraphics*, **37** 2164–2180. PMID: 29028423, <https://doi.org/10.1148/rg.2017170037>, URL <https://doi.org/10.1148/rg.2017170037>.
- JUNG, W., JUNG, D., KIM, B., LEE, S., RHEE, W. and AHN, J. H. (2019). Restructuring batch normalization to accelerate cnn training. In *Proceedings of Machine Learning and Systems* (A. Talwalkar, V. Smith and M. Zaharia, eds.), vol. 1. 14–26. URL <https://proceedings.mlsys.org/paper/2019/file/6f4922f45568161a8cdf4ad2299f6d23-Paper.pdf>.
- KALLAS, M., FRANCIS, C., KANAAN, L., MERHEB, D., HONEINE, P. and AMOUD, H. (2012). Multi-class SVM classification combined with kernel PCA feature extraction of ECG signals. In *2012 19th International Conference on Telecommunications (ICT)*. 1–5.
- KANAN, T., SADAQA, O., ALDAJEH, A., ALSHWABKA, H., AL-DOLIME, W., ALZU’BI, S., ELBES, M., HAWASHIN, B. and ALIA, M. A. (2019). A review of natural language processing and machine learning tools used to analyze arabic social media. In *2019 IEEE Jordan International Joint Conference on Electrical Engineering and Information Technology (JEEIT)*. 622–628.
- KIMELDORF, G. and WAHBA, G. (1971). Some results on Tchebycheffian spline functions. *Journal of Mathematical Analysis and Applications*, **33** 82–95.
- KINGMA, D. P. and BA, J. (2014). Adam: A method for stochastic optimization. URL <https://arxiv.org/abs/1412.6980>.
- KUMAR, A., SARAWAGI, S. and JAIN, U. (2018). Trainable calibration measures for neural networks from kernel mean embeddings. In *Proceedings of the 35th International Conference on Machine Learning*. Stockholm, Sweden, 10.
- KURTZER, G. M., SOCHAT, V. and BAUER, M. W. (2017). Singularity: Scientific containers for mobility of compute. *PLOS ONE*, **12** 1–20. URL <https://doi.org/10.1371/journal.pone.0177459>.

- LABACH, A., SALEHINEJAD, H. and VALAEE, S. (2019). Survey of dropout methods for deep neural networks. URL <https://arxiv.org/abs/1904.13310>.
- LI, Q., CAI, W., WANG, X., ZHOU, Y., FENG, D. D. and CHEN, M. (2014). Medical image classification with convolutional neural network. In *2014 13th International Conference on Control, Automation, Robotics and Vision (ICARCV)*. 844–848.
- LI, X., ZHANG, G., HUANG, H. H., WANG, Z. and ZHENG, W. (2016). Performance analysis of GPU-based convolutional neural networks. In *2016 45th International Conference on Parallel Processing (ICPP)*. 67–76.
- LIN, Y., LEE, Y. and WAHBA, G. (2002). Support vector machines for classification in non-standard situations. *Machine Learning*, **46** 191–202.
- LITJENS, G., KOOI, T., BEJNORDI, B. E., SETIO, A. A. A., CIOMPI, F., GHAFOORIAN, M., VAN DER LAAK, J. A., VAN GINNEKEN, B. and SÁNCHEZ, C. I. (2017). A survey on deep learning in medical image analysis. *Medical Image Analysis*, **42** 60–88.
- LOWE, D. (1999). Object recognition from local scale-invariant features. In *Proceedings of the Seventh IEEE International Conference on Computer Vision*, vol. 2. 1150–1157 vol.2.
- LOWE, D. G. (2004). Distinctive image features from scale-invariant keypoints. *International Journal of Computer Vision*, **60** 91–110. URL <https://doi.org/10.1023/B:VISI.0000029664.99615.94>.
- LUQUE, A., MAZZOLENI, M., CARRASCO, A. and FERRAMOSCA, A. (2022). Visualizing classification results: Confusion star and confusion gear. *IEEE Access*, **10** 1659–1677.
- LUTZ, C., BRESS, S., RABL, T., ZEUCH, S. and MARKL, V. (2018). Efficient and scalable k-Means on GPUs. *Datenbank-Spektrum*, **18** 157–169. URL <https://doi.org/10.1007/s13222-018-0293-x>.
- MANNING, C. D., RAGHAVAN, P. and SCHÜTZE, H. (2008). *Introduction to Information Retrieval*. Cambridge University Press.

- MINDERER, M., DJOLONGA, J., ROMIJNDERS, R., HUBIS, F., ZHAI, X., HOULSBY, N., TRAN, D. and LUCIC, M. (2021). Revisiting the calibration of modern neural networks. In *Advances in Neural Information Processing Systems*, vol. 34. 15682–15694. URL <http://arxiv.org/abs/2106.07998>.
- NAEINI, M. P., COOPER, G. F. and HAUSKRECHT, M. (2015). Obtaining well calibrated probabilities using bayesian binning. *AAAI Conference on Artificial Intelligence*, **2015** 2901–2907.
- NEARY, P. (2018). Automatic hyperparameter tuning in deep convolutional neural networks using asynchronous reinforcement learning. In *2018 IEEE International Conference on Cognitive Computing (ICCC)*. 73–77.
- RUSSAKOVSKY, O., DENG, J., SU, H., KRAUSE, J., SATHEESH, S., MA, S., HUANG, Z., KARPATY, A., KHOSLA, A., BERNSTEIN, M., BERG, A. C. and FEI-FEI, L. (2015). ImageNet large scale visual recognition challenge. *International Journal of Computer Vision*, **115** 211–252. URL <https://doi.org/10.1007/s11263-015-0816-y>.
- SAJJAD, M., KHAN, S., MUHAMMAD, K., WU, W., ULLAH, A. and BAIK, S. W. (2019). Multi-grade brain tumor classification using deep CNN with extensive data augmentation. *Journal of Computational Science*, **30** 174–182. URL <https://www.sciencedirect.com/science/article/pii/S1877750318307385>.
- SANTOS, F. F. D., PIMENTA, P. F., LUNARDI, C., DRAGHETTI, L., CARRO, L., KAELI, D. and RECH, P. (2019). Analyzing and increasing the reliability of convolutional neural networks on gpus. *IEEE Transactions on Reliability*, **68** 663–677.
- SHARIF, M., AMIN, J., SIDDIQA, A., KHAN, H. U., ARSHAD MALIK, M. S., ANJUM, M. A. and KADRY, S. (2020). Recognition of different types of leukocytes using yolov2 and optimized bag-of-features. *IEEE Access*, **8** 167448–167459.
- SIVIC, J. and ZISSERMAN, A. (2003). Video google: a text retrieval approach to object matching in videos. *Proceedings Ninth IEEE International Conference on Computer Vision* 1470–1477 vol.2.

- SULTAN, H. H., SALEM, N. M. and AL-ATABANY, W. (2019). Multi-classification of brain tumor images using deep neural network. *IEEE Access*, **7** 69215–69225.
- SULTANA, F., SUFIAN, A. and DUTTA, P. (2018). Advancements in image classification using convolutional neural network. In *2018 Fourth International Conference on Research in Computational Intelligence and Communication Networks (ICRCICN)*. 122–129.
- THANAPOL, P., LAVANGNANANDA, K., BOUVRY, P., PINEL, F. and LEPRÉVOST, F. (2020). Reducing overfitting and improving generalization in training convolutional neural network (cnn) under limited sample sizes in image recognition. In *2020 - 5th International Conference on Information Technology (InCIT)*. 300–305.
- TOMAR, D. and AGARWAL, S. (2015). A comparison on multi-class classification methods based on least squares twin support vector machine. *Knowledge-Based Systems*, **81** 131–147. URL <https://linkinghub.elsevier.com/retrieve/pii/S0950705115000520>.
- TUBA, E., BAČANIN, N., STRUMBERGER, I. and TUBA, M. (2021). *Artificial Intelligence: Theory and Applications*, chap. Convolutional neural networks hyperparameters tuning. Springer, New York, New York, USA, 65–84.
- VAN ROSSUM, G. and DRAKE, F. L. (2009). *Python 3 Reference Manual*. CreateSpace, Scotts Valley, CA. URL <https://docs.python.org/3/reference/>.
- WAHBA, G. (1990). Spline models for observational data. In *CBMS-NSF Regional Conference Series. SIAM Society for Industrial and Applied Mathematics*.
- WANG, G., LI, W., ZULUAGA, M. A., PRATT, R., PATEL, P. A., AERTSEN, M., DOEL, T., DAVID, A. L., DEPREST, J., OURSELIN, S. and VERCAUTEREN, T. (2018). Interactive medical image segmentation using deep learning with image-specific fine tuning. *IEEE Transactions on Medical Imaging*, **37** 1562–1573.
- WANG, J., SHEN, X. and LIU, Y. (2008). Probability estimation for large margin classifiers. *Biometrika*, **95** 149–167.

- WANG, J., YANG, J., YU, K., LV, F., HUANG, T. and GONG, Y. (2010). Locality-constrained linear coding for image classification. In *2010 IEEE Computer Society Conference on Computer Vision and Pattern Recognition*. 3360–3367.
- WANG, X., ZHANG, H. H. and WU, Y. (2019). Multiclass probability estimation with support vector machines. *Journal of Computational and Graphical Statistics*, **28** 586–595. URL <https://www.tandfonline.com/doi/full/10.1080/10618600.2019.1585260>.
- WERNICK, M. N., YANG, Y., BRANKOV, J. G., YOURGANOV, G. and STROTHER, S. C. (2010). Machine learning in medical imaging. *IEEE Signal Processing Magazine*, **27** 25–38.
- WOOD, S. N., PYA, N. and SÄFKEN, B. (2016). Smoothing parameter and model selection for general smooth models. *Journal of the American Statistical Association*, **111** 1548–1563. URL <https://www.tandfonline.com/doi/full/10.1080/01621459.2016.1180986>.
- WU, Y., ZHANG, H. H. and LIU, Y. (2010). Robust model-free multiclass probability estimation. *Journal of the American Statistical Association*, **105** 424–436.
- WU, Z. and YU, J. (2019). Vector quantization: a review. *Frontiers of Information Technology & Electronic Engineering*, **20** 507–524. URL <http://link.springer.com/10.1631/FITEE.1700833>.
- YADAV, S. S. and JADHAV, S. M. (2019). Deep convolutional neural network based medical image classification for disease diagnosis. *Journal of Big Data*, **6** 113. URL <https://doi.org/10.1186/s40537-019-0276-2>.
- YU, K., ZHANG, T. and GONG, Y. (2009). Nonlinear Learning using Local Coordinate Coding. In *Advances in Neural Information Processing Systems* (Y. Bengio, D. Schuurmans, J. Lafferty, C. Williams and A. Culotta, eds.), vol. 22. Curran Associates, Inc. URL <https://proceedings.neurips.cc/paper/2009/file/2afe4567e1bf64d32a5527244d104cea-Paper.pdf>.
- ZENG, L. and ZHANG, H. H. (2022). Linear algorithms for robust and scalable nonparametric

multiclass probability estimation. *Journal of Data Science*, **21** 658–680. URL <https://jds-online.org/journal/JDS/article/1305/info>.